Phase relations in the system MgSiO$_3$–Al$_2$O$_3$ up to 52 GPa and 2000 K

Zhaodong Liu [a],[*],[1], Tetsuo Irifune [a],[b], Masayuki Nishi [a],[b], Yoshinori Tange [b],[c], Takeshi Arimoto [a], Toru Shinmei [a]

[a] Geodynamics Research Center (GRC), Ehime University, Japan
[b] Earth-Life Science Institute (ELSI), Tokyo Institute of Technology, Japan
[c] SPring-8, Japan Synchrotron Radiation Institute, Japan

ARTICLE INFO

ABSTRACT

Phase relations in the system MgSiO$_3$–Al$_2$O$_3$ have been determined for pressures from 15 to 52 GPa and at a temperature of 2000 K from *in situ* synchrotron X-ray diffraction measurements obtained using sintered diamond anvils in a multi-anvil apparatus. A wide two-phase region of garnet and corundum is found to exist up to 27 GPa; at higher pressures, a phase assemblage of aluminous bridgmanite and corundum is stabilized. The solubility of Al$_2$O$_3$ in bridgmanite and that of MgSiO$_3$ in corundum are highly dependent on pressure; the Al$_2$O$_3$ content in bridgmanite increases from 12 mol% at 27 GPa to 29 mol% at 52 GPa, forming bridgmanite with the pyrope composition (25 mol% Al$_2$O$_3$) at about 45 GPa. In contrast, the MgSiO$_3$ content in corundum decreases from 24 mol% at 27 GPa to 9 mol% at 52 GPa. The minimum pressure where the pyropic bridgmanite is formed is significantly higher than the result of the earlier study ($\sim$37 GPa) on the pyrope composition. These results suggest the Al$_2$O$_3$ content in bridgmanite and the MgSiO$_3$ content in corundum are good pressure indicators in the mixed-phase region at pressures above 30 GPa, where virtually no pressure references are available for quench experiments. The new phase diagram in the system MgSiO$_3$–Al$_2$O$_3$ confirms that bridgmanite is the dominant host mineral for Al$_2$O$_3$ in the pyrolitic or peridotitic compositions under the pressure and temperature conditions of the Earth's lower mantle.

1. Introduction

Bridgmanite (MgSiO$_3$ perovskite) is widely accepted to be the most abundant mineral in the Earth's lower mantle and thereby the entire Earth (Liu, 1976; Ito and Matsui, 1978; Mao et al., 1991; Irifune, 1994; Tschauner et al., 2014). The presence of Al$_2$O$_3$ has been reported to significantly affect the stability field of bridgmanite (Kesson et al., 1995; Irifune et al., 1996; McCammon, 1997). Moreover, Al$_2$O$_3$ has been demonstrated to change considerably the electrical conductivity (Xu et al., 1998), and elastic properties (e.g., Zhang and Weidner, 1999; Murakami et al., 2012) of bridgmanite. Therefore, clarifying the effect of Al$_2$O$_3$ on the stability and physical properties of bridgmanite is of great significance in geophysics.

Some previous experiments indicated that the solubility of Al$_2$O$_3$ in bridgmanite is very limited and a separate Al-rich phase

may exist in the lower mantle (Ito and Takahashi, 1987; Ahmed-Zaïd and Madon, 1995), whereas more recent studies (Irifune, 1994; Irifune et al., 1996; O'Neill and Jeanloz, 1990; Kesson et al., 1995; Wood, 2000) reported that such an Al-rich phase is absent in the lower mantle. Phase relations in the system MgSiO$_3$–Al$_2$O$_3$, which is a simplified model most relevant to the chemical composition of the lower mantle (Irifune et al., 1996; Irifune and Tsuchiya, 2007), have been extensively studied using the multi-anvil apparatus with tungsten carbide (WC) anvils to understand the behavior of Al$_2$O$_3$ under the lower mantle conditions (Irifune et al., 1996; Kubo and Akaogi, 2000; Hirose et al., 2001; Akaogi et al., 2002). However, these studies are restricted to pressures below 27 GPa because of the limitations in the hardness of WC anvils used in the second-stage anvils of the multi-anvil apparatus. It was found that bridgmanite can accommodate Al$_2$O$_3$ up to about 17 mol% at 27 GPa and 2073 K, equivalent to the pressure and temperature conditions of the uppermost part of the lower mantle (Irifune et al., 1996), but the Al$_2$O$_3$ solubility in bridgmanite remains unclear at pressures of the deeper region of the lower mantle. Bridgmanite with a composition close to pyrope (pyropic bridgmanite; containing 25 mol% Al$_2$O$_3$) was suggested to be

formed at 37 GPa and 1873 K (Ito et al., 1998) through quench experiments using a multi-anvil apparatus experiments, whereas laser-heated diamond anvil cell experiments on pyropic samples indicated that pyropic bridgmanite is formed at pressures above 43 GPa (Kesson et al., 1995; Serghiou et al., 1998; Kondo and Yagi, 1998). On the other hand, theoretical calculations predicted that pyropic bridgmanite is formed at higher pressures of 65–80 GPa at 1900–2000 K (Panero et al., 2006; Tsuchiya and Tsuchiya, 2008; Kawai and Tsuchiya, 2015).

Developments of high-pressure techniques using sintered diamond (SD) anvils combined with *in situ* synchrotron X-ray diffraction observations in a multi-anvil apparatus enable precise determinations of high-pressure phase transitions to be performed at pressures up to 60 GPa and temperatures up to 2273 K, equivalent to intermediate regions of the lower mantle (Tange et al., 2008, 2009). Applying this high-pressure technique, we conducted a series of high-pressure and high-temperature experiments to clarify phase relations in the system $MgSiO_3$–Al_2O_3 under the deep lower mantle conditions.
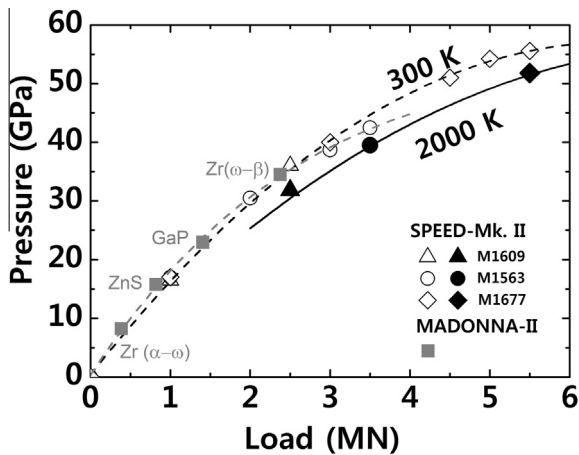

Fig. 1. The generated pressures versus the press loads at room temperature (300 K, open symbols) and 2000 K (filled symbols) for *in situ* X-ray diffraction experiments using a DIA-type apparatus (SPEED-MK.II) at SPring-8. The dashed and solid lines represent the fitting results of the data at 300 and 2000 K, respectively. The gray symbols represent the room pressure calibration in MADONNA-II at GRC (gray symbols, Stagno et al., 2011), and the gray dashed line represents their fitting result.

2. Experimental methods

We used a starting material of fine-grained oxide mixture of $En_{50}Cor_{50}$ (En: $MgSiO_3$, Cor: Al_2O_3) composition for the present high-pressure experiments. A glass with the pyrope composition ($En_{75}Cor_{25}$, hereafter "pyropic glass") was also used to ensure a chemical equilibrium of phases appearing at high pressure and high temperature. Three glasses with En_{100}, $En_{95}Cor_5$, and En_{90}-Cor_{10} compositions were additionally used to check the generated pressures and the consistency with earlier studies. The $En_{50}Cor_{50}$ oxide mixture was prepared from reagent-grade chemicals of MgO, SiO_2, and Al_2O_3 with very fine grain sizes of ~50 nm to enhance the chemical reaction. All starting materials were confirmed to have the intended chemical composition within the analytical uncertainties using electron microprobe analyses (see Supplementary Table S1). We tried to minimize the effect of adsorbed water on the phase relations; the individual fine-grained chemicals were firstly heated to 1000 °C in an oven for one hour, and then mixed together in an agate mortar under ethanol for 3 h. The glass was quenched from the molten oxide mixture at 2073 K under atmospheric pressure, then ground into fine powders under ethanol for 3 h. These starting materials and all parts of the high-pressure cell assembly were dried in a vacuum oven at 393 K in preparation for the high-pressure and high-temperature experiments. The starting material was firstly loaded into a graphite capsule on a hot plate, dried in an oven, and then put into the high-pressure cell assembly on a hot plate. The details of the cell assembly used for the present high pressure and high temperature runs are the same as those reported previously (Tange et al., 2008, 2009; Stagno et al., 2011; Nishi et al., 2013).

High-pressure quench experiments at 15–27 GPa (e.g., OS2699 run) were conducted using WC anvils with an 8/3 (OEL/TEL = Octahedral Edge Length of pressure medium/Truncated Edge Length of anvil) cell assembly in a multi-anvil apparatus (Orange-2000) at the Geodynamics Research Center, Ehime University. Pressure of these quench experiments was calibrated against press loads based on the phase transitions of GaAs (18.7 GPa) and GaP (23 GPa) at room temperature (Irifune et al., 1996). Pressures at high temperature in these quench experiments were evaluated based on the pressures for ilmenite to bridgmanite transition in $MgSiO_3$ (~23 GPa) and the decomposition of pyrope into aluminous bridgmanite and corundum (~27 GPa) at ~2000 K (Kubo and Akaogi,

Table 1
Experimental conditions and phases present.

Run No.	Starting sample	Pressure (GPa)	Temperature (K)	Duration (h)	Decomposed phases
OS2705	$En_{50}Cor_{50}$ oxide	15	2000	2.5	Gar + Cor + tr (Sti)
OS2722	"	23	"	3	Gar + Cor + tr (Sti)
OS2703	"	25	["]	"	Gar + Cor + tr (Sti)
OS2723	"	27	"	"	Al-Brg + Cor + tr (Ga + Sti)
OS2772	"	27	["]	12	Al-Brg + Cor
M1609	"	31.8	"	3	Al-Brg + Cor
MII-251	"	37.8	["]	"	Al-Brg + Cor
MII-257	"	45.0	"	"	Al-Brg + Cor + tr (Sti)
M1677	"	51.8	"	"	Al-Brg + Cor + tr (Sti)
M1564	"	31.9	1700	"	Al-Brg + Cor
OS2723	$En_{75}Cor_{25}$ glass	27	2000	12	Al-Brg + Cor + tr (Sti)
M1609	"	31.8	"	3	Al-Brg + Cor + tr (Sti)
MII-257	"	45.0	"	"	Al-Pv* + tr (Sti)
M1677	"	51.8	"	"	Al-Pv* + tr (Sti)
OS2722	En_{100} glass	23	"	"	Al-Brg
OS2703	$En_{95}Cor_5$ glass	25	"	"	Al-Brg
MII-274	"	24	"	0.5	Al-Brg + Gar
OS2772	$En_{90}Cor_{10}$ glass	27	"	12	Al-Brg

" Same with above.
[] Temperature was evaluated form a calibrated power curve derived from previous experiments.
Abbreviations: Gar: garnet, Cor: corundum, Sti: stishovite, Al-Brg: aluminous bridgmanite, Al-Pv*: aluminous perovskite with $LiNbO_3$ structure, tr: trace.

2000). The pressure uncertainties of these quench experiments were estimated at ±0.5 GPa (Irifune et al., 1996).

Experiments at higher pressures of 31.8–51.8 GPa were performed using SD anvils with TEL = 1.5 mm as the second-stage anvils in the two DIA-type multi-anvil apparatuses (SPEED-Mk. II at SPring-8 and MADONNA-II Geodynamics Research Center), which are virtually the identical apparatus made by the same company (Sumitomo Heavy Industries, Ltd., Japan). In situ X-ray diffraction measurements were carried out using the energy-dispersive method with a Ge solidstate detector in SPEED-Mk. II multi-anvil apparatus (Katsura et al., 2004; Tange et al., 2009). The diffraction angle (2θ) was fixed at about 6°, which was calibrated using the X-ray diffraction peaks of Au. The generated pressure at room temperature and 2000 K were evaluated in three in situ runs at SPring-8 (Fig. 1). We lost one sample of M1563 (in situ run) at 37.8 GPa and 2000 K when opening this strongly deformed recovered sample because of a small blow-out occur during decompression; however, we can calibrate pressures accurately using the in situ X-ray diffraction peaks of Au for this run. The pressure of the in situ X-ray diffraction experiments was determined based on the equation of state of Au (Tsuchiya, 2003), which was mixed with the starting materials. The pressure uncertainties for in situ X-ray diffraction experiments are about ±0.2 GPa, arising mainly as a consequence of errors in molar volume measurements of Au. Based on these precise pressure measurements for in situ X-ray diffraction experiments, two additional quench experiments (MII-251 and MII-257) were also conducted with SD anvils in

MADONNA-II multi-anvil apparatus. The pressure calibration for MADONNA-II was also conducted at room temperature by monitoring semiconductor to metal transitions or phase transitions in Zr (α–ω transition at 8 GPa), ZnS (15.6 GPa), GaP (22 GPa) and Zr (ω–β transition at 34 GPa) as reported by Tange et al. (2011) and Stagno et al. (2011), which is consistent with that through the in situ X-ray diffraction study at room temperature for SPEED-Mk. II in both Stagno et al. (2011) and the present study (Fig. 1). Hence, we believe the accuracies of the pressures in these two runs are similar to those based on in situ X-ray diffraction measurements, as we used essentially the same cell assembly and high-pressure apparatus in these experiments (Stagno et al., 2011). Temperature was measured with a $W_{97}Re_3$-$W_{75}Re_{25}$ thermocouple, the hot junction of which was placed at the center of the cell assembly.

The sample was firstly compressed to the target pressure, and heated at 2000 K for 3 h. Then, the run was quenched by turning off the electronic power, and the pressure was released slowly over several hours. The recovered sample was mounted in the epoxy resin, ground to expose the centered portion and then polished using 1 μm diamond paste. The microstructure observation and chemical composition analysis of the recovered sample were made by a Field-Emission Scanning Electron Microscopy (FE-SEM; JEOLJSM-7000F) equipped with an energy dispersive spectrometer (EDS). The EDS analysis was calibrated against $MgSiO_3$ enstatite, Mg_2SiO_4 forsterite and Al_2O_3 corundum standards. Quenched products were also examined using a micro-focus X-ray diffractometer
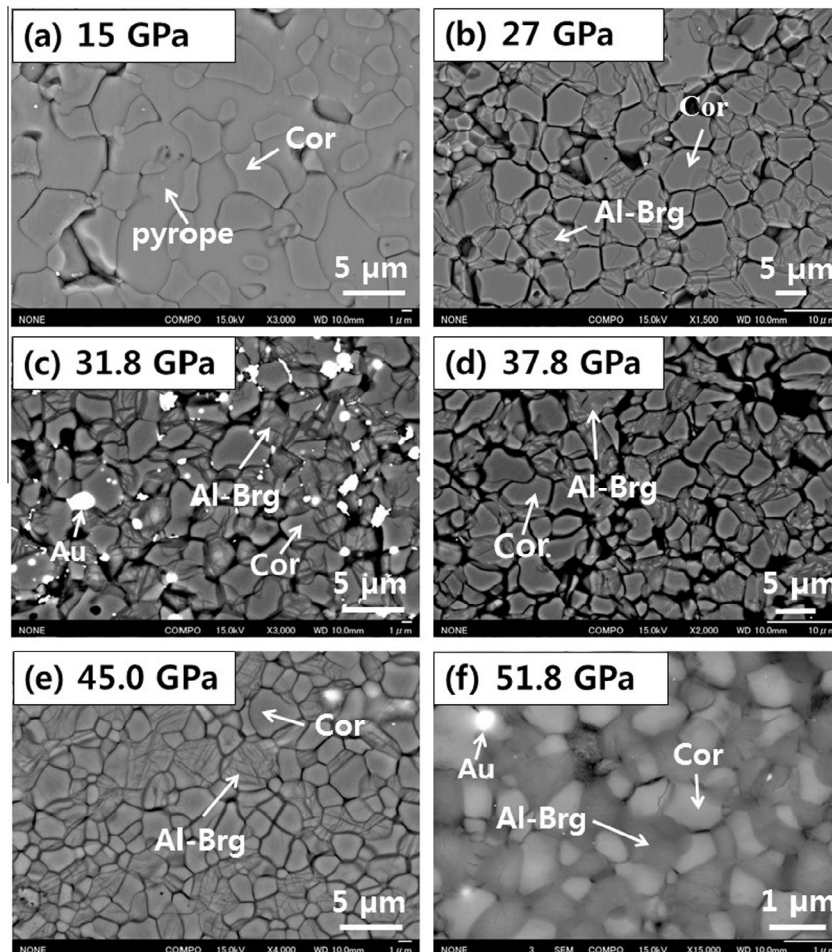

Fig. 2. Representative back-scattered electron images of the run products for $En_{50}Cor_{50}$ synthesized at pressures from 15 to 51.8 GPa at 2000 K. Abbreviations: Al-Brg, aluminous bridgmanite; Cor, corundum.

with a rotating Cu anode operated at 40 kV, 30 mA. High-purity Si and $MgSiO_3$ bridgmanite were used as the external standards to calibrate the Bragg angle (2θ) of the instrument. The X-ray diffraction profile of the recovered sample was collected over 1 h.

3. Results

Experimental conditions and results of the present runs are summarized in Table 1. The temperature for the high-pressure experiments is set at 2000 K, which is close to a typical adiabatic mantle geotherm in the Earth's lower mantle (Brown and Shankland, 1981). The mineral phases in the recovered samples were identified from X-ray diffraction measurements. Representative electron back-scattering images of the quenched samples for $En_{50}Cor_{50}$ are shown in Fig. 2 and the chemical compositions of mineral phases in the recovered samples are summarized in Table 2; the corresponding X-ray diffraction profiles of the quenched samples are presented in Fig. 3. Both Fig. 2 and 3 show that $En_{50}Cor_{50}$ decomposes to pyrope and Al_2O_3-rich corundum at 15–25 GPa, and corundum is found to contain some amount of $MgSiO_3$, which increases from ~8 mol% at 15 GPa to ~18 mol% at 25 GPa. At 27 GPa, an assemblage of aluminous bridgmanite (containing ~12 mol% Al_2O_3) and corundum (containing ~23 mol% $MgSiO_3$) appears as a result of a disproportionation of pyrope. An additional run (OS2772) was made with a longer heating duration of 12 h at the same pressure and temperature condition as that in OS2723, yielding mutually consistent chemical compositions for aluminous bridgmanite and corundum (Table 2). This result indicates the chemical equilibrium is achieved in 3 h for our $En_{50}Cor_{50}$ sample at high-pressure and high-temperature (see below for further discussion).

Using SD anvils for the higher pressure experiments, between 31.8 and 51.8 GPa, the coexistence of aluminous bridgmanite and corundum is found in the recovered samples. At 31.8 GPa, bridgmanite dissolves ~18 mol% Al_2O_3 and corundum contains ~20 mol% $MgSiO_3$. As pressure is increased to 45.0 GPa, aluminous bridgmanite with the Al_2O_3 content close to that of pyrope is formed, whereas the $MgSiO_3$ content in corundum decreases by ~3 mol% compared with that at 31.8 GPa. At 51.8 GPa, quenched products are aluminous bridgmanite and corundum with grain size of ~1 μm, and we were unable to get accurate chemical compositions of the phases in this run product because of the limitations in the spatial resolution of the EDS analysis using FE-SEM.

Fig. 4. shows *in situ* synchrotron X-ray diffraction patterns for $En_{50}Cor_{50}$ under 31.8 and 51.8 GPa at 2000 K, respectively. In all X-ray diffraction patterns, the major reflections are assigned to those of bridgmanite, corundum and Au pressure markers, while the other minor peaks originate from stishovite, surrounding diamond capsules, and MgO disks. The stability of pyropic bridgmanite in the present study is within the pressure range (up to 140 GPa and 2200 K) reported by Tateno et al. (2005). After quenching, the intensity of aluminous bridgmanite peaks become weaker than

Table 2
Chemical compositions of the coexisting mineral phases in the run products at pressures of 15–51.8 GPa at 2000 K.

	OS2705 (15 GPa)		OS2722 (23 GPa)		OS2703 (25 GPa)		OS2723 (27 GPa)	
	Gar ($n = 15$)	Cor ($n = 13$)	Gar ($n = 10$)	Cor ($n = 11$)	Gar ($n = 8$)	Cor ($n = 9$)	Brg ($n = 10$)	Cor ($n = 12$)
MgO	30.54 (38)	3.59 (85)	30.11 (43)	6.03 (21)	31.02 (78)	7.55 (15)	35.64 (147)	10.06 (83)
Al_2O_3	26.19 (91)	92.71 (179)	24.42 (138)	83.49 (191)	24.00 (60)	83.36 (66)	13.05 (177)	78.21 (187)
SiO_2	43.81 (71)	4.42 (107)	43.34 (32)	8.79 (76)	44.80 (89)	10.67 (23)	51.30 (116)	13.85 (96)
Total	100.55 (86)	100.73 (108)	97.86 (92)	98.31 (198)	99.82 (121)	101.57 (86)	99.99 (148)	102.11(81)
No. of Oxygens	12	12	12	12	12	12	12	12
Mg	3.044 (40)	0.361 (85)	3.081 (49)	0.620 (27)	3.111 (44)	0.748 (11)	3.566 (118)	0.993 (86)
Al	2.064 (72)	7.361 (148)	1.976 (103)	6.779 (62)	1.906 (64)	6.550 (21)	1.034 (145)	6.114 (146)
Si	2.931 (37)	0.297 (70)	2.978 (55)	0.606 (50)	3.014 (34)	0.712 (11)	3.444 (52)	0.918 (66)
Sum.	8.039 (11)	8.019 (14)	8.035 (11)	8.005 (23)	8.031 (16)	8.010(0)	8.044 (25)	8.025 (7)
	OS2772 (27 GPa)[a]		M1564 (31.9 GPa)[b]		M1609 (31.8 GPa)		MII-251 (37.8 GPa)	
	Brg ($n = 10$)	Cor ($n = 14$)	Brg ($n = 9$)	Cor ($n = 8$)	Brg ($n = 14$)	Cor ($n = 27$)	Brg ($n = 21$)	Cor ($n = 17$)
MgO	37.37 (71)	10.99 (40)	34. 86 (69)	6.01 (33)	33.31 (83)	8.26 (62)	32.61 (117)	5.74 (23)
Al_2O_3	11.48 (32)	77.65 (105)	13.67 (62)	86.78 (63)	18.67 (126)	82.14 (141)	20.00 (154)	86.98 (80)
SiO_2	54.10 (42)	15.15 (54)	52.41 (64)	8.63 (38)	48.93 (98)	11.57 (71)	47.62 (147)	8.46 (19)
Total	102.91 (107)	103.31 (71)	100.95 (150)	101.41 (103)	100.75 (147)	101.97 (71)	100.23 (128)	101.18 (83)
No. of Oxygens	12	12	12	12	12	12	12	12
Mg	3.625 (38)	1.067 (37)	3.440 (36)	0.600 (25)	3.318 (68)	0.816 (59)	3.254 (11)	0.572 (23)
Al	0.883 (24)	5.968 (78)	1.080 (44)	6.27 (41)	1.478 (102)	6.432 (101)	1.579 (126)	6.864 (23)
Si	3.525 (31)	0.988 (40)	3.473 (30)	0.573 (21)	3.232 (63)	0.766 (48)	3.187 (72)	0.566(13)
Sum.	8.033 (21)	8.023 (5)	7.993 (30)	8.000 (25)	8.028 (23)	8.014 (8)	8.020 (42)	8.002 (10)
	MII-257 (45.0 GPa)		MII-257[*] (45.0 GPa)		M1677[*] (51.8 GPa)	OS2772[*] (27 GPa)	OS2703[*] (25 GPa)	OS2722[*] (23 GPa)
	Brg ($n = 30$)	Cor ($n = 41$)	Brg ($n = 10$)	Brg ($n = 11$)	Brg ($n = 8$)	Brg ($n = 6$)	Brg ($n = 6$)
MgO	30.04 (99)	5.98 (90)	30.01 (71)	29.41 (58)	36.98 (73)	38.95 (56)	40.32 (36)
Al_2O_3	26.41 (118)	86.90 (179)	25.11 (59)	24.84 (23)	10.07 (38)	5.28 (17)	
SiO_2	45.73 (125)	8.46 (127)	46.00 (71)	45.99 (98)	54.01 (131)	56.42 (85)	57.88 (58)
Total	102.18 (136)	101.35(136)	101.12 (116)	100.24 (147)	101.06 (199)	100.65 (104)	98.20 (34)
No. of Oxygens	12	12	12	12	12	12	12
Mg	2.958 (104)	0.595 (85)	2.964 (56)	2.927 (41)	3.656 (34)	3.867 (54)	4.100 (49)
Al	2.022 (144)	6.849 (163)	1.960 (38)	1.954 (20)	0.788 (32)	0.414(14)	
Si	3.003 (62)	0.565 (80)	3.048 (44)	3.071 (27)	3.580 (28)	3.757 (27)	3.950 (24)
Sum.	7.982 (20)	8.009 (9)	7.972 (32)	7.952 (21)	8.024 (18)	8.039(26)	8.050 (24)

n: number of analysis points.
Number in parentheses represents standard deviation and is placed in the last digit (s).
Abbreviations: Gar: garnet; Brg, bridgmanite; Cor, corundum.
  [*] Glass starting materials.
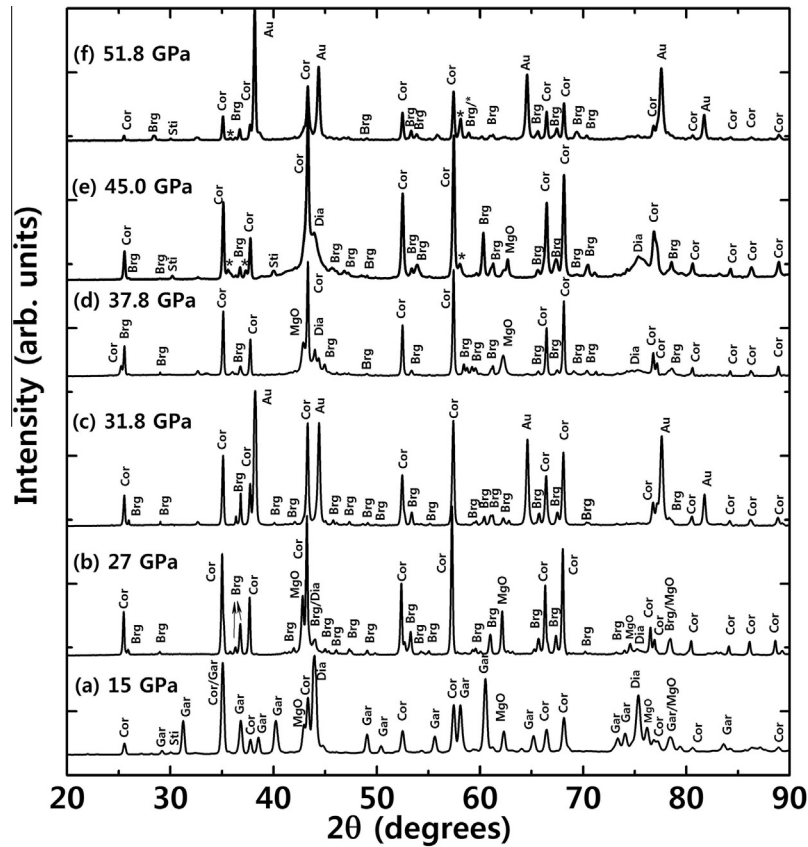 [a] Heating time of 12 h.
  [b] The run at 1700 K.

Fig. 3. X-ray diffraction patterns of the quenched products for En$_{50}$Cor$_{50}$ synthesized at pressures of 15–51.8 GPa at 2000 K. The stars indicate the peaks of the LiNbO$_3$ structure (Ko and Prewitt, 1988) for perovskite at ambient conditions. Abbreviations: Brg, bridgmanite; Cor, corundum; Gar, garnet; Dia, diamond.
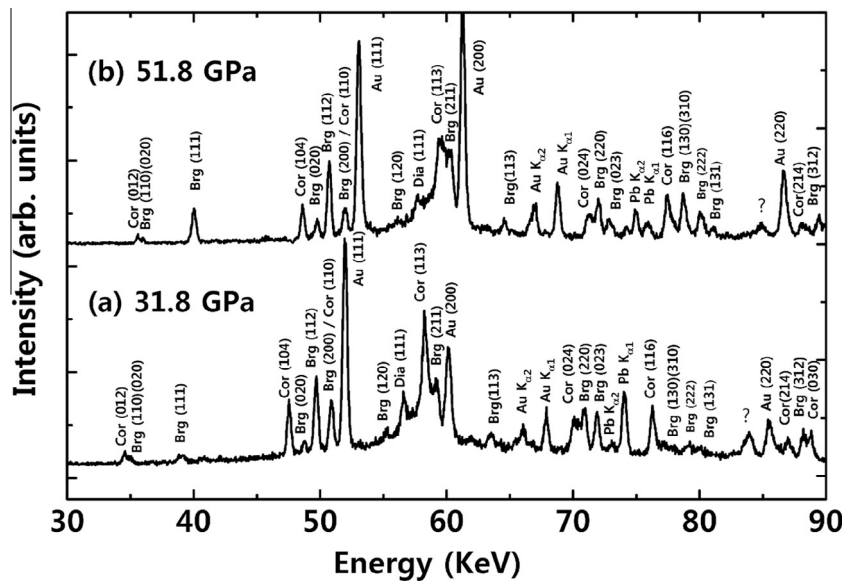

Fig. 4. Examples of *in situ* X-ray diffraction profiles of run products under high pressures at 2000 K. Abbreviations: Brg, bridgmanite; Cor, corundum; Dia, diamond.

those of corundum (Fig. 3) in a comparison of peak intensities for those at the *in situ* X-ray diffraction patterns (Fig. 4). This variation of peak intensity for aluminous bridgmanite may be the result of partial amorphization at ambient conditions. For X-ray diffraction peaks of the run products quenched from 27 to 37.8 GPa, the main peaks can be indexed into those of bridgmanite, corundum, and other adjacent phases (e.g., diamond and MgO). For the run prod-

ucts quenched from 45.0 to 51.8 GPa, a few unknown peaks appeared (Fig. 3), in addition to the main peaks of bridgmanite and corundum. We found these peaks are well explained by the diffractions from the LiNbO$_3$-like structure with a rhombohedral symmetry. This result suggests that bridgmanite with an Al$_2$O$_3$ content more than 25 mol% would have mostly transformed into the LiNbO$_3$ structure upon releasing pressure, which is consistent
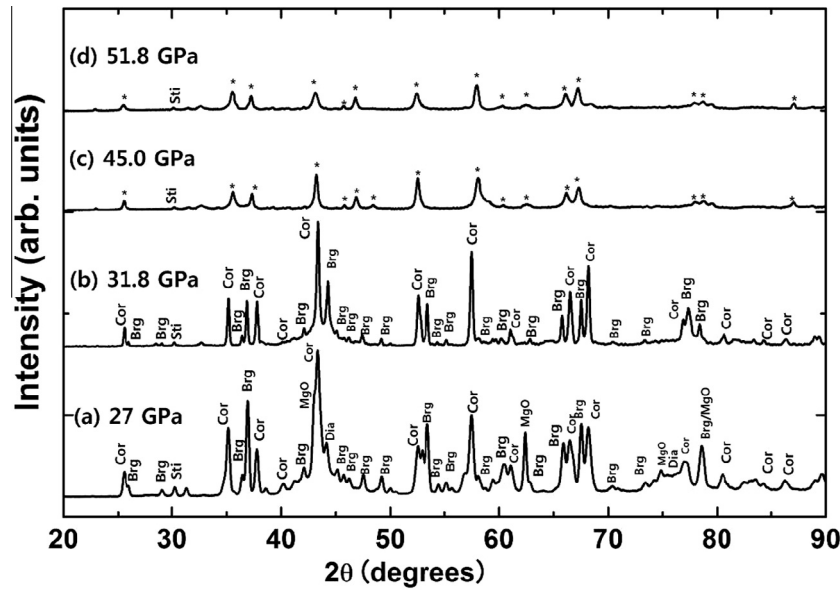
Fig. 5. X-ray diffraction patterns of the quenched products for pyropic glass at pressures of 27–51.8 GPa at 2000 K. The stars indicate the peaks of the LiNbO₃ structure (Ko and Prewitt, 1988) converted from bridgmanite during decompression. Abbreviations: Brg, bridgmanite; Cor, corundum; Gar, garnet; Dia, diamond.

Table 3
The lattice parameters of the coexisting phases for the pyropic glasses at pressures of 27–51.8 GPa and the oxide mixture for M1677.

Run	OS2723 (27 GPa)		M1609 (31.8 GPa)		MII-257 (45 GPa)	M1677 (51.8 GPa)	M1677⁺ (51.8 GPa)		Funamori et al. (1997)
Lattice parameters	Al-Brg	Cor	Al-Brg	Cor	Al-Pv*	Al-Pv*	Al-Brg	Cor	Al-Pv*
a/Å	4.777 (2)	4.762 (1)	4.779 (5)	4.767 (1)	4.815 (1)	4.818 (3)	4.783 (2)	4.767 (2)	4.837 (1)
b/Å	4.936 (1)	″	4.943 (8)	″	″	″	4.960 (5)	″	″
c/Å	6.939 (3)	12.995 (5)	6.943 (7)	13.001 (9)	12.665 (2)	12.680 (12)	6.963 (11)	13.000 (9)	12.733 (7)

″Same with above.
Abbreviations: Al-Brg: aluminous bridgmanite, Cor: corundum, Al-Pv*: aluminous perovskite with LiNbO₃ structure.
  ⁺ The run using the oxide mixture as the starting material.

with an earlier result reporting that perovskite containing an Al₂O₃ content of 25–28 mol% transformed into a mixture of orthorhombic perovskite and LiNbO₃ phase (Miyajima et al., 1999).

Supplementary Fig. S1 shows the back-scattered electron images of the run products for pyropic glass as starting material, which was loaded into the same cell assembly with the En₅₀Cor₅₀ oxide mixture, at various pressures. At 27 and 31.8 GPa, bridgmanite and corundum can be clearly identified in the X-ray diffraction profiles in Fig. 5, although they cannot be distinguished by the contrast in the back-scattered electron image of the recovered sample because their grain sizes are less than ~1 μm and they have close atomic numbers. The lattice parameters of bridgmanite and corundum for pyropic glass at 27 and 31.8 GPa (Table 3) were evaluated using about ten reflections of these two phases. At 45.0 GPa, the composition of perovskite is identical with that of the starting pyropic glass within the analytical uncertainties (Table 2), which is further confirmed by the element mapping (Supplementary Fig. S2). This "perovskite" with the pyrope composition (pyropic perovskite) is not bridgmanite [MgSiO₃ in the orthorhombic ABO₃ perovskite structure (Tschauner et al., 2014)] but has a LiNbO₃ structure with rhombohedral symmetry at ambient conditions. This pyropic perovskite with the LiNbO₃ structure is also found in the recovered sample from the run at 51.8 GPa. The present result for the pyropic glass is consistent with that reported by Funamori et al. (1997), who found that the pyropic bridgmanite transforms into the LiNbO₃ structure after decompression from ~60 GPa, suggesting that this pyropic perovskite is formed by the back transformation of bridgmanite during decompression. The

unit-cell parameters of the pyropic perovskite with the LiNbO₃ structure are smaller than those for Funamori et al. (1997) due to the presence of Ca and Fe, for which the ionic radii are larger than that of Mg, in their sample (Table 3). Compared with the results for the En₅₀Cor₅₀ oxide, where the bridgmanite structure is preserved upon releasing the pressure, the complete conversion to the LiNbO₃ structure in the samples using the glass starting material may be caused by the effect of nanoscale grain size with a higher surface energy (Tolbert and Alivisatos, 1994) in these samples.

As shown in Fig. 6, both the Mg and Si content of bridgmanite decrease with increasing pressure up to 45.0 GPa, whereas the Al content of bridgmanite increases concomitantly, which is in contrast to the variation of these cations for corundum. In Fig. 7, the trends expected for the two competing substitutional mechanisms [the charge-coupled substitution (Al³⁺ + Al³⁺ = Mg²⁺ + Si⁴⁺) and the oxygen vacancy substitution (2Si⁴⁺ + O²⁻ = 2Al³⁺ + V₍Ö₎; where V₍Ö₎ means an oxygen vacancy)] for bridgmanite (Hirsch and Shankland, 1991; Richmond and Brodholt, 1998; Navrotsky, 1999; Navrotsky et al., 2003; Brodholt, 2000; Yamamoto et al., 2003; Walter et al., 2004) are compared using the chemical compositions of bridgmanite in the present and previous studies (Irifune et al., 1996; Kubo and Akaogi, 2000; Navrotsky et al., 2003). Both Figs. 6 and 7 indicate that the Mg/Si ratios in bridgmanite at various pressures are close to unity within the analytical errors, and significantly lower than those of the defect perovskites along the MgSiO₃–MgAlO₂.₅ join (Navrotsky et al., 2003) [Fig. 7(a)], suggesting that the charge-coupled substitution is more favorable than the competing oxygen vacancy substitution in aluminous bridgmanite
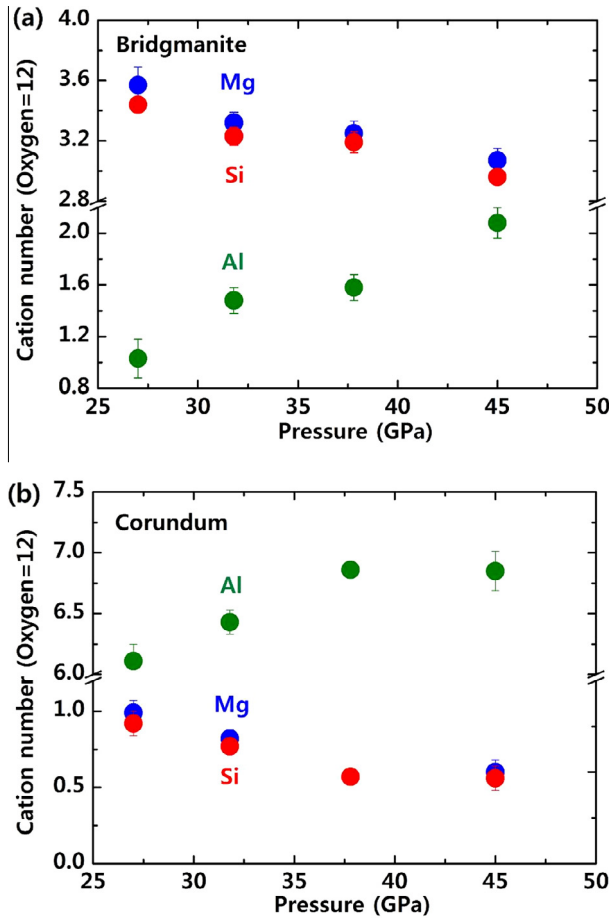
Fig. 6. Variations of the cation number of aluminous bridgmanite (a) and corundum (b) as a function of pressures at 2000 K. The number of oxygen atoms is fixed to 12 for both aluminous bridgmanite and corundum. The blue, red and green circles represent the number of Mg, Si and Al in the phases, respectively. (For interpretation of the references to color in this figure legend, the reader is referred to the web version of this article.)

Fig. 7. (a) The relationship between Mg/Si and Al^{3+} contents in bridgmanite in the present and previous studies (Irifune et al., 1996; Kubo and Akaogi, 2000;Navrotsky et al., 2003). Concentrations are per formula unit (PFU) of $MgSiO_3$ bridgmanite. (b) The Si cation content versus the total Al^{3+} cation content for Al-bearing bridgmanite. Solid lines indicate the trends expected for trivalent cation incorporation by the charge-coupled substitution mechanism, and the dashed line represents the oxygen vacancy mechanism. Solid circles indicate the results in the present study. Open squares, trigonal and circles are data from Irifune et al. (1996), Kubo and Akaogi (2000) and Navrotsky et al. (2003), respectively.

at these pressures, especially for bridgmanite containing high alumina content (Kubo and Akaogi, 2000; Walter et al., 2004, 2006). Fig. 7(b) further verify this point because the bridgmanite composition plot is mainly along the trend line for the charge-coupled substitution within the analytical uncertainties, especially for the alumina-rich bridgmanite. This idea is consistent with the results of some earlier work on aluminous bridgmanite (Kubo and Akaogi, 2000; Stebbins et al., 2001; Yamamoto et al., 2003; Walter et al., 2004, 2006).

In contrast, the occurrence of trace stishovite is also observed in some runs in the present study, suggesting that the oxygen vacancy substitution may also occur in aluminous bridgmanite. In fact, the formation of stishovite was also encountered in earlier studies (Ito et al., 1998; Kubo and Akaogi, 2000). Thus, we cannot completely rule out the possibility of the occurrence of oxygen vacancy substitution in the present products as we also observed trace amounts of stishovite appearing in some recovered samples. We believe though that this mechanism would play only a minor role in the Al-rich region and at the very high pressures studied, consistent with an earlier *ab initio* study (Brodholt, 2000). Further studies are needed to clarify the relationship between these two substitution mechanisms in bridgmanite under various pressures, temperatures, and Al_2O_3 contents.

Fig. 8. shows the unit-cell lattice parameters of aluminous bridgmanite and corundum as a function of the Al_2O_3 content, respectively. The lattice parameters (*b*- and *c*-axes) of bridgmanite
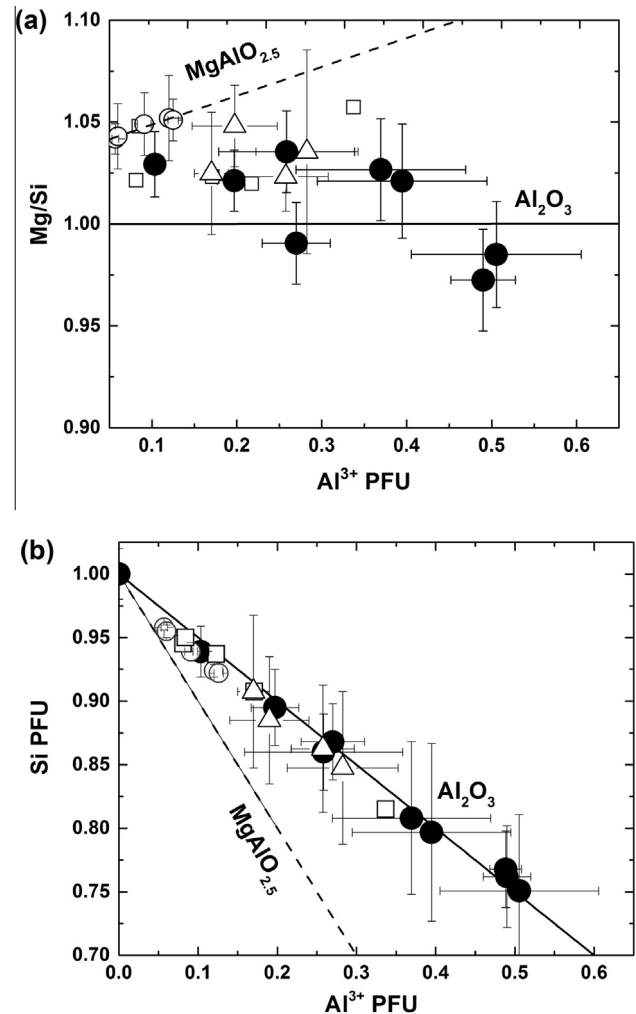
increase almost linearly with increasing Al_2O_3 contents [Fig. 8(a)], whereas those of the *a*-axis do not change significantly. These lattice parameter data of aluminous bridgmanite are well fitted by the following linear equations:

$$a = 4.776\ (\pm 0.001) + 0.021\ (\pm 0.011) \times \chi_{Al2O3}$$
$$b = 4.926\ (\pm 0.003) + 0.127\ (\pm 0.014) \times \chi_{Al2O3}$$
$$c = 6.897\ (\pm 0.002) + 0.258\ (\pm 0.031) \times \chi_{Al2O3}$$

where χ_{Al2O3} represents the mole fraction of the Al_2O_3 in bridgmanite ($0 \leqslant \chi_{Al2O3} \leqslant 0.26$). These relations are generally consistent with those in the previous studies within the uncertainties (Irifune et al., 1996; Ito and Matsui, 1978), although the slopes for the change in lattice parameters with the Al_2O_3 content for bridgmanite are slightly smaller than those in earlier studies (Irifune et al., 1996; Ito and Matsui, 1978). This discrepancy may have originated with the different synthesis conditions or the presence of small amounts of water (Kubo and Akaogi, 2000).

Moreover, as the end members of $MgSiO_3$ ilmenite (trigonal, $R\bar{3}$) and Al_2O_3 corundum (trigonal, $R\bar{3}$) possess the same symmetry

with the different space groups (Horiuchi et al., 1982; D'Amour et al., 1978), the lattice parameters of solid solutions in the system $MgSiO_3$ ilmenite–Al_2O_3 corundum in the present study and previous studies (Liu, 1977; Ito and Matsui, 1977; D'Amour et al., 1978; Irifune et al., 1996; Akaogi et al., 2002) are also illustrated in Fig. 8(b). It is seen that the lattice parameters of the c-axis for Al_2O_3 corundum slightly increase with increasing $MgSiO_3$ contents, whereas those of the a-axis do not change significantly. Because the grains of the samples recovered at 51.8 GPa were very small, the Al_2O_3 content ($\sim$29 ± 5 mol%) in bridgmanite and the $MgSiO_3$ content ($\sim$9 ± 3 mol%) in corundum in this run are evaluated from the relationship between the lattice parameters (Table 3) and chemical compositions of bridgmanite and corundum in Fig. 8.

4. Discussion

Fig. 9. depicts the phase relations in the $MgSiO_3$–Al_2O_3 system at pressures up to 52 GPa at 2000 K based on the present high-pressure experiments. The results of earlier studies (Irifune et al., 1996; Kubo and Akaogi, 2000; Panero et al., 2006) are also shown for comparison. A phase assemblage of pyrope and corundum is stabilized at pressures below 27 GPa, where corundum dissolves more $MgSiO_3$ contents with increasing pressure. At pressures above 27 GPa, a two-phase field of aluminous bridgmanite and corundum is formed, where bridgmanite and corundum become more aluminous with increasing pressure. The Al_2O_3 content in bridgmanite increases form $\sim$12 mol% at 27 GPa to $\sim$29 mol% at 51.8 GPa, while the Al_2O_3 content in corundum increases from $\sim$75 mol% to $\sim$85 mol% in this pressure range. In addition, the mutual solubilities of Al_2O_3 and $MgSiO_3$ in bridgmanite and corundum, respectively, seem to be lower at lower temperatures,

as suggested by the results for the M1564 run at 31.9 GPa and 1700 K (Fig. 9).

To further constrain the phase relations determined by the above results using $En_{50}Cor_{50}$ oxide mixture, pyropic glass is used as a starting material for experiments with the same pressure and temperature conditions as those for the $En_{50}Cor_{50}$ oxide mixture. Based on the composition-lattice parameter relationships, the estimated Al_2O_3 content ($\sim$9 ± 5 mol%) in bridgmanite and the $MgSiO_3$ content ($\sim$26 ± 2 mol%) in corundum for pyropic glass is close to those for $En_{50}Cor_{50}$ at 27 GPa (the A_2O_3 content in bridgmanite:$\sim$11 ± 1 mol%; the $MgSiO_3$ content in corundum:$\sim$25 ± 1 mol%). At 31.8 GPa, the chemical compositions of these phases for pyropic glass are also consistent with those for the oxide mixture within analytical uncertainties (Fig. 9). At 45.0 GPa, the pure pyropic bridgmanite forms, which is also consistent with the result for the oxide mixture at the same pressure. Thus, the phase boundaries constrained by the results with different starting materials of $En_{50}Cor_{50}$ oxide mixture and pyropic glass are mutually consistent (Table 2), indicating that the chemical equilibrium is achieved in the present high-pressure runs at 2000 K for 3 h. It should be also noted that the result with a longer heating duration of 12 h (Run OS2772) agrees with that of the shorter duration of 3 h for a corresponding run (OS2723).

The phase boundary between bridgmanite and the mixture of bridgmanite and corundum in the system $MgSiO_3$–Al_2O_3 at pressures up to 52 GPa at 2000 K shifts toward higher pressures compared with those based on quench experiments at 1873 K (Ito et al., 1998). In the present study, pyrope is found to undergo a phase transition to bridgmanite and corundum at 27 GPa, and then to a single phase of pyropic bridgmanite at approximately 45 GPa, whereas this pressure is significantly higher than that
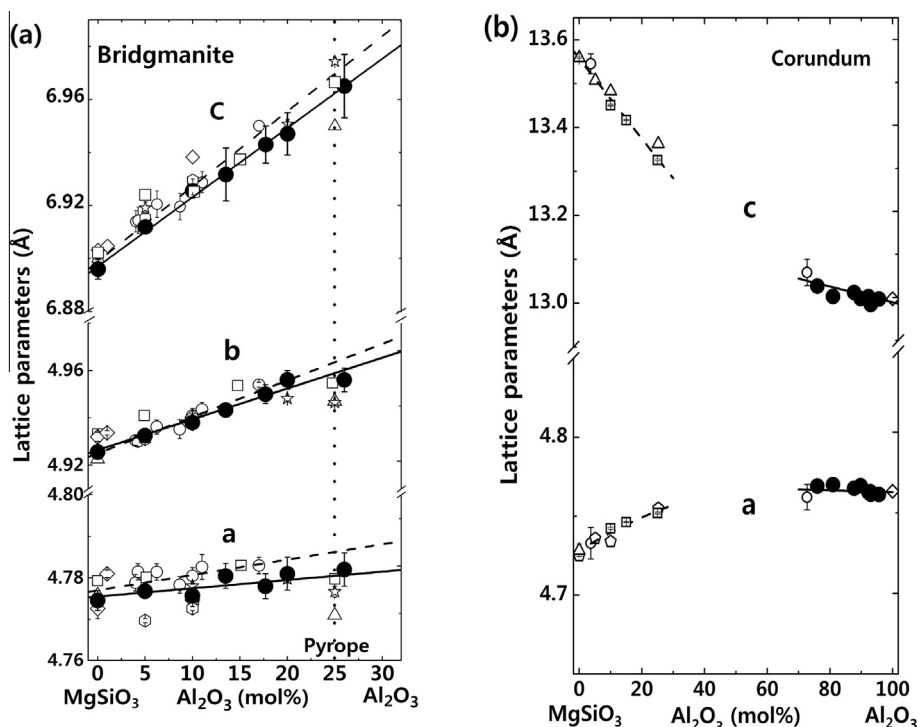

Fig. 8. (a) Lattice parameters of aluminous bridgmanite in the system $MgSiO_3$–Al_2O_3. Solid circles indicate the results in the present study. Open trigonal, squares, circles, diamonds, stars and hexagon are data from Ito and Matsui (1978), Ito et al. (1998), Weng et al. (1981), Irifune et al. (1996), Yagi et al. (2004) and Walter et al. (2004), respectively. The solid lines represent the fitting result of the present data. The dashed lines indicate previous results. The dotted line indicates the chemical composition of pyrope. (b) Lattice parameters of ilmenite and corundum in the system $MgSiO_3$–Al_2O_3. Solid circles indicate results in the present study. Open hexagon, trigonal, diamonds, circles and squares are data from Liu (1977), Ito and Matsui (1977), D'Amour et al. (1978), Irifune et al. (1996) and Akaogi et al. (2002), respectively. The solid lines represent the fitting results of the present data and those from D'Amour et al. (1978) and Irifune et al. (1996), while the dashed lines represent those of previous studies on ilmenite. The error bars indicate the uncertainties of the lattice parameters.
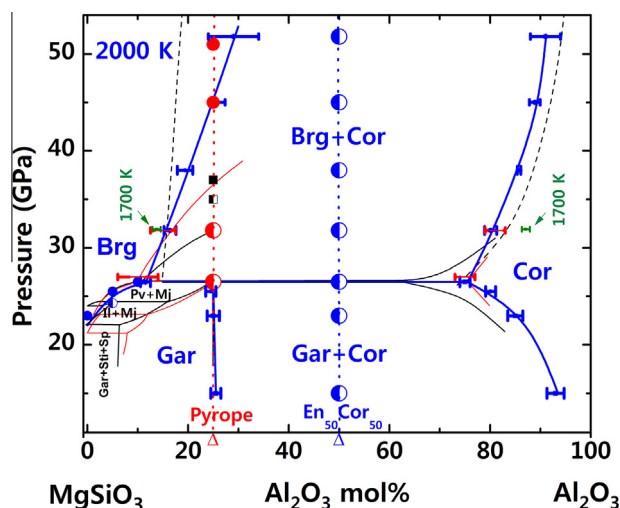
Fig. 9. Phase relations in the MgSiO₃–Al₂O₃ system at 15–52 GPa and 2000 K (solid blue lines). Solid black and red lines represent previous work on the phase relations in the same system up to 27 GPa and 1773 (Irifune et al., 1996) and 1873 K (Kubo and Akaogi, 2000), respectively. Dashed black lines indicate the theoretical calculated phase boundaries at pressures above 27 GPa at 2000 K (Panero et al., 2006). Dotted blue and red lines represent the chemical composition of the starting materials in the present study. Large blue circular symbols indicate the high pressure runs using the En₅₀Cor₅₀ oxide mixture, while large red circular symbols indicate those for the pyropic glass. Blue horizontal-lined symbols mark the compositions of the coexisting phases for En₅₀Cor₅₀ oxide mixture, and those of olivine symbols indicate the compositions of the phases at 1700 K. Red horizontal-lined symbols mark the compositions of the coexisting phases for pyropic glass. Smaller blue circles indicate the run products at various high pressure and high temperature using the glasses containing 0, 5, and 10 mol% Al₂O₃ content as the starting material (Supplementary Fig. S3). Black squares are data from Ito et al. (1998). Error bars indicate the uncertainties of chemical compositions of the coexisting phases. Abbreviations: Brg, bridgmanite; Cor, corundum; Gar, garnet; Il, ilmenite; Sp, spinel. (For interpretation of the references to color in this figure legend, the reader is referred to the web version of this article.)

(37 GPa at 1873 K) of Ito et al. (1998). As a few minor peaks of corundum are seen in the X-ray diffraction pattern of the recovered sample, we believe that pure pyropic bridgmanite was not formed at this pressure and temperature in the latter study. It should be also noted Ito et al. (1998) did not report the chemical compositions of the recovered samples as the grain size of the products were too small for electron microprobe analysis. In contrast, we evaluated the run pressures using *in situ* X-ray diffraction measurements, and also checked the chemical equilibrium of the phases present using different starting materials and electron microprobe analyses on the run products. In addition, the lattice parameters of bridgmanite quenched from 37 GPa and 1827 K in Ito et al. (1998) are comparable to those of bridgmanite synthesized in our MII251 run (37.8 GPa and 2000 K), suggesting that the Al₂O₃ content in the former study may be similar to that of latter study (Fig. 8). Indeed, theoretical studies (Panero et al., 2006; Tsuchiya and Tsuchiya, 2008; Kawai and Tsuchiya, 2015) predicted that the phase boundary pressures are much higher than the result of Ito et al. (1998). Moreover, Serghiou et al. (1998) and Kondo and Yagi (1998) also suggested that pyropic bridgmanite should form at pressures above 43 GPa based on laser-heated diamond anvil cell experiments. Therefore, pyropic bridgmanite should form at higher pressure of about 45 GPa, as demonstrated in the present study.

For the quench experiments, the pressure calibration of the multi-anvil apparatus is crucial to simulate the Earth's interior conditions. The phase transitions of some reference materials and minerals (e.g., GaAs, GaP, MgSiO₃ and pyrope) have been widely used to estimate the pressures up to 27 GPa at room temperature

and high temperatures in the quench experiments (Irifune et al., 1996; Kubo and Akaogi, 2000; Hirose et al., 2001). At pressures above 27 GPa, the candidates of Zr (34 GPa, Tange et al., 2011) and Fe₂O₃ (58 GPa, Ito et al., 2009) have been used as pressure references in experiments at room temperature; however, pressure calibration at high temperatures are scant for the higher-pressure quench experiments. The present phase relations in the system MgSiO₃–Al₂O₃ at pressures above 27 GPa suggest that the Al₂O₃ content in bridgmanite increases progressively with increasing pressure, whereas the MgSiO₃ content in corundum decreases gradually with increasing pressure. Hence, the Al₂O₃ content in bridgmanite and the MgSiO₃ content in corundum determined in this new phase diagram for 2000 K provide good pressure indicators at pressures above 27 GPa in high-pressure quench experiments, where no adequate pressure references are available at high temperature.

Some previous studies suggested that several Al-rich phases are formed in the mantle materials under the lower mantle conditions. Ito and Takahashi (1987) reported that a separate Al-rich phase coexisted with bridgmanite in peridotite and basalt compositions. Ahmed-Zaïd and Madon (1995) reported that two Al-rich phases of MgAl₂SiO₆ with unknown structures and Al₂SiO₅ with the V₃O₅ structure coexisted with bridgmanite for the natural pyrope garnet in the lower mantle conditions. Irifune et al. (1991) found another Al-rich phase with the calcium ferrite structure, while Miyajima et al. (1999) reported a new hexagonal phase with a composition close to (Mg, Fe, Ca, Na, K)₃Al₄Si₁.₅O₁₂, which is different from those in Ito and Takahashi (1987) and Ahmed-Zaïd and Madon (1995). A more recent study by Irifune et al. (1996) suggested that the Al-rich phases in earlier studies by Ito and Takahashi (1987) and Ahmed-Zaïd and Madon (1995) were in fact corundum solid solutions. The entire Al₂O₃ is accommodated into bridgmanite in the upper part of the pyrolite or peridotite lower mantle, and no other Al-rich phases exist in this region (Irifune, 1994; Irifune et al., 1996). Our new phase relations in the system MgSiO₃–Al₂O₃ further support this conclusion that no separate Al-rich phase exists in this system under the pressure and temperature conditions of the uppermost to the middle regions of the lower mantle, and all Al₂O₃ is accommodated into bridgmanite in the pyrolite or peridotite compositions in this region of the lower mantle.

Appendix A. Supplementary data

Supplementary data associated with this article can be found, in the online version, at http://dx.doi.org/10.1016/j.pepi.2016.05.006.

References

Ahmed-Zaïd, I., Madon, M., 1995. Electron microscopy of high pressure phases synthesized from natural garnets in a diamond anvil cell: implications for the mineralogy of the lower mantle. Earth Planet. Sci. Lett. 129, 233–247.

Akaogi, M., Tanaka, A., Ito, E., 2002. Garnet–ilmenite–perovskite transitions in the system Mg₄Si₄O₁₂–Mg₃Al₂Si₃O₁₂ at high pressures and high temperatures: phase equilibria, calorimetry and implications for mantle structure. Phys. Earth Planet. Inter. 132, 303–324.

Brown, J.M., Shankland, T.J., 1981. Thermodynamic parameters in the Earth as determined from seismic profiles. Geophys. J. R. Astron. Soc. 66, 579–596.

Brodholt, J.P., 2000. Pressure-induced changes in the compression mechanism of aluminous perovskite in the Earth's mantle. Nature 407, 620–622.

D'Amour, H., Schiferl, D., Denner, W., Schulz, H., Holzapfel, W.B., 1978. High-pressure single-crystal structure determinations for ruby up to 90 kbar using an automatic diffractometer P = 0 kbar. J. Appl. Phys. 49, 4411–4416.

Funamori, N., Yagi, T., Miyajima, N., Fujino, K., 1997. Transformation in garnet: from orthorhombic perovskite to LiNbO$_3$ phase on release of pressure. Science 275, 513–515.

Hirose, K., Fei, Y., Yagi, T., Funakoshi, K., 2001. In situ measurements of the phase transition boundary in Mg$_3$Al$_2$Si$_3$O$_{12}$: implications for the nature of the seismic discontinuities in the Earth's mantle. Earth Planet. Sci. Lett. 184, 567–573.

Hirsch, L.M., Shankland, T.J., 1991. Point defects in silicate perovskite. Geophys. Res. Lett. 18, 1305–1308.

Horiuchi, H., Hirano, M., Ito, E., Matsui, Y., 1982. MgSiO$_3$ (ilmenite-type): single crystal X-ray diffraction study. Am. Mineral. 67, 788–793.

Irifune, T., Fujino, K., Fujino, K., Ohtani, E., 1991. A new high-pressure form of MgAl$_2$O$_4$. Nature 349, 409–411.

Irifune, T., 1994. Absence of an aluminous phase in the upper part of the Earth's lower mantle. Nature 370, 131–133.

Irifune, T., Koizumi, T., Ando, J., 1996. An experimental study of the garnet-perovskite transformation in the system MgSiO$_3$-Mg$_3$Si$_3$O$_{12}$. Phys. Earth Planet. Inter. 96, 147–157.

Irifune, T., Tsuchiya, T., 2007. Phase transition and mineralogy of the lower mantle. In: Price, G.D. (Ed.), Treatise on Geophysics, 2. Elsevier, pp. 33–62.

Ito, E., Matsui, Y., 1977. Silicate ilmenite and the post-spinel transformations. In: Manghnani, M.H., Akimoto, S. (Eds.), High-Pressure Research: Applications in Geophysics. Academic Press, New York, pp. 193–208.

Ito, E., Matsui, Y., 1978. Synthesis and crystal–chemical characterization of MgSiO$_3$ perovskite. Earth Planet. Sci. Lett. 38, 443–450.

Ito, E., Takahashi, E., 1987. Ultra high-pressure phase transformations and the constitution of the deep mantle. In: Syono, Y., Manghnani, M.H. (Eds.), High-Pressure Research: Application to Earth and Planetary Sciences. Terra, American Geophysical Union, Tokyo, Washington, DC, pp. 221–229.

Ito, E., Kubo, A., Katsura, T., Akaogi, M., Fujita, T., 1998. High-pressure transformation of pyrope (Mg$_3$Al$_2$Si$_3$O$_{12}$) in a sintered diamond cubic anvil assembly. Geophys. Res. Lett. 25, 821–824.

Ito, E., Katsura, T., Yamazaki, D., Yoneda, A., Tado, M., Ochi, T., Nishibara, E., Nakamura, A., 2009. A new 6-axis apparatus to squeeze the Kawai-cell of sintered diamond cubes. Phys. Earth Planet. Inter. 174, 264–269.

Katsura, T., Funakoshi, K., Kubo, A., Nshiyama, N., Tange, Y., Sueda, Y., Kubo, T., Utsumi, W., 2004. A large-volume high-pressure and high-temperature apparatus for in situ X-ray observation, SPEED-Mk. II. Phys. Earth Planet. Inter. 143–144, 497–506.

Kawai, K., Tsuchiya, T., 2015. Elasticity and phase stability of pyrope garnet from ab initio computation. Phys. Earth Planet. Inter. 240, 125–131.

Kesson, S.E., Fitzgerald, J.D., Shelley, J.M.G., Withers, R.L., 1995. Phase relations, structure and crystal chemistry of some aluminous perovskites. Earth Planet. Sci. Lett. 134, 187–201.

Ko, J., Prewitt, C.T., 1988. High-pressure phase transition in MnTiO$_3$ from the ilmenite to the LiNbO$_3$ structure. Phys. Chem. Miner. 15, 355–362.

Kondo, T., Yagi, T., 1998. Phase transition of pyrope garnet under lower mantle conditions. In: Manghnani, M.H., Yagi, T. (Eds.), Properties of Earth and Planetary Materials at High Pressure and Temperature, 101. Am. Geophys. Union, Geophys. Monogr., pp. 419–427.

Kubo, A., Akaogi, M., 2000. Post-garnet transitions in the system Mg$_4$Si$_4$O$_{12}$-Mg$_3$Al$_2$Si$_3$O$_{12}$ up to 28 GPa: phase relations of garnet, ilmenite and perovskite. Phys. Earth Planet. Inter. 121, 85–102.

Liu, L.G., 1976. Orthorhombic perovskite phases observed in olivine, pyroxene, and garnet at high pressures and temperatures. Phys. Earth Planet. Inter. 11, 289–298.

Liu, L.G., 1977. The system enstatite–pyrope at high pressures and temperatures and the mineralogy of the earth's mantle. Earth Planet. Sci. Lett. 36, 237–245.

Mao, H.K., Hemley, R.J., Fei, Y., Shu, J.F., Chert, L.C., Jephcoat, A.P., Wu, Y., 1991. Effect of pressure, temperature, and composition on lattice parameters and density of (Fe, Mg)SiO$_3$ perovskites to 30 GPa. J. Geophys. Res. 96 (B5), 8069–8077.

McCammon, C.A., 1997. Perovskite as a possible sink for ferric iron in the lower mantle. Nature 387, 694–696.

Miyajima, N., Fujino, K., Funamori, N., Kondo, T., Yagi, T., 1999. Garnet–perovskite transformation under conditions of the Earth's lower mantle: an analytical transmission electron microscopy study. Phys. Earth Planet. Inter. 116, 117–131.

Murakami, M., Ohishi, Y., Hirao, N., Hirose, K., 2012. A perovskitic lower mantle inferred from high-pressure, high-temperature sound velocity data. Nature 485, 90–94.

Navrotsky, A., 1999. A lesson from ceramics. Science 284, 1788–1789.

Navrotsky, A., Schoenitz, M., Kojitani, H., Xu, H., Zhang, J., Weidener, D.J., Jeanloz, R., 2003. Aluminum in magnesium silicate perovskite: formation, structure, and energetics of magnesium-rich defect solid solutions. J. Geophys. Res. 108, 2330.

Nishi, M., Nishihara, Y., Irifune, T., 2013. Growth kinetics of MgSiO$_3$ perovskite reaction rim between stishovite and periclase up to 50 GPa and its implication for grain boundary diffusivity in the lower mantle. Earth Planet. Sci. Lett. 377–378, 191–198.

O'Neill, B., Jeanloz, R., 1990. Experimental petrology of the lower mantle: a natural peridotite taken to 54 GPa. Geophys. Res. Lett. 77, 1477–1480.

Panero, W.R., Akber-Knutson, S., Stixrude, L., 2006. Al$_2$O$_3$ incorporation in MgSiO$_3$ perovskite and ilmenite. Earth Planet. Sci. Lett. 252, 152–161.

Richmond, N.C., Brodholt, J.P., 1998. Calculated role of aluminum in the incorporation of ferric iron into magnesium silicate perovskite. Am. Mineral. 83, 947–951.

Serghiou, G., Zerr, A., Chopelas, A., Boehler, R., 1998. The transition of pyrope to perovskite. Phys. Chem. Miner. 25, 193–196.

Stagno, V., Tange, Y., Miyajima, N., McCammon, C.A., Irifune, T., Frost, D.J., 2011. The stability of magnesite in the transition zone and the lower mantle as function of oxygen fugacity. Geophys. Res. Lett. 38, L19309.

Stebbins, J.F., Kroeker, S., Andrault, D., 2001. The mechanism of solution of aluminum oxide in MgSiO$_3$ perovskite. Geophys. Res. Lett. 28, 615–618.

Tange, Y., Irifune, T., Funakoshi, K., 2008. Pressure generation to 80 GPa using multianvil apparatus with sintered diamond anvils. High Pressure Res. 28, 245–254.

Tange, Y., Takahashi, E., Nishihara, Y., Funakoshi, K., Sata, N., 2009. Phase relations in the system MgO-FeO-SiO$_2$ to 50 GPa and 2000°C: an application of experimental techniques using multianvil apparatus with sintered diamond anvils. J. Geophys. Res. 114, B02214.

Tange, Y., Takahashi, E., Funakoshi, 2011. In situ observation of pressure-induced electrical resistance changes in zirconium: pressure calibration points for the large volume press at 8 and 35 GPa. High Pressure Res. 31, 413–418.

Tateno S., Hirose, K., Sata, N., Ohishi, Y., 2005. Phase relation in Mg$_3$Al$_2$Si$_3$O$_{12}$ to 180 GPa: effect of Al on post-perovskite phase transition. Geophys. Res. Lett. 32, L15306.

Tolbert, S.H., Alivisatos, A.P., 1994. Size dependence of a first order solid–solid phase transition: the wurtzite to rock salt transformation in CdSe nanocrystals. Science 265 (5170), 373–376.

Tschauner, O., Ma, C., Beckett, J.R., Precher, C., Prakapenka, V.R., Rossman, G.R., 2014. Discovery of bridgmanite, the most abundant mineral in Earth, in a shocked meteorite. Science 346, 1100–1101.

Tsuchiya, T., 2003. First-principles prediction of the P-V-T equation of state of gold and the 660-km discontinuity in Earth's mantle. J. Geophys. Res. 108, B10.

Tsuchiya, T., Tsuchiya, J., 2008. Postperovskite phase equilibria in the MgSiO$_3$–Al$_2$O$_3$ system. Natl. Acad. Sci. USA 105, 19180–19164.

Walter, M., Kubo, A., Yoshino, T., Brodholt, J., Koga, K.T., Ohishi, Y., 2004. Phase relations and equation-of-state of aluminous Mg-silicate perovskite and implications for Earth's lower mantle. Earth Planet. Sci. Lett. 222, 501–516.

Walter, M., Tronnes, R.G., Armstrong, L.S., Lord, O., Caldwell, W.A., Clark, A.M., 2006. Subsolidus phase relations and perovskite compressibility in the system MgO-AlO$_{1.5}$-SiO$_2$ with implications for Earth's lower mantle. Earth Planet. Sci. Lett. 248, 77–89.

Weng, K., Mao, H.K., Bell, P.M., 1981. Lattice Parameters of the Perovskite Phase in the System MgSiO$_3$–CaSiO$_3$–Al$_2$O$_3$, 81. Carnegie Inst. Year Book, Washington, pp. 273–277.

Wood, B.J., 2000. Phase transformations and partitioning relations in peridotite under lower mantle conditions. Earth Planet. Sci. Lett. 174, 341–354.

Xu, Y., McCammon, C.A., Poe, B.T., 1998. The effect of alumina on the electrical conductivity of silicate perovskite. Science 282, 922–924.

Yagi, T., Okabe, K., Nishiyama, N., Kubo, A., Kikegawa, T., 2004. Complicated effects of aluminum on the compressibility of silicate perovskite. Phys. Earth Planet. Inter. 143–144, 81–89.

Yamamoto, T., Yuen, D.A., Ebisuzaki, T., 2003. Substitution mechanism of Al ions in MgSiO$_3$ perovskite under high pressure conditions from first-principles calculations, Earth Planet. Sci. Lett. 206, 617–625.

Zhang, J., Weidner, D.J., 1999. Thermal equation of state of aluminum-enriched silicate perovskite. Science 284, 782–784.